Nanoscale

PAPER

View Article Online
View Journal | View Issue

Cite this: *Nanoscale*, 2022, **14**, 17735

Enhancement of self-trapped excitons and near-infrared emission in Bi^{3+}/Er^{3+} co-doped $Cs_2Ag_{0.4}Na_{0.6}InCl_6$ double perovskite†

Kashyap Dave, [a,b] Wen-Tse Huang, [a] Tadeusz Leśniewski, [c] Agata Lazarowska, [c] Maciej Grzegorczyk, [c] Sebastian Mahlik, [c] Grzegorz Leniec, [d] Sławomir M. Kaczmarek [d] and Ru-Shi Liu *[a]

Received 3rd October 2022,
Accepted 17th November 2022

DOI: 10.1039/d2nr05478g

rsc.li/nanoscale

Erbium (Er) complexes are used as optical gain materials for signal generation in the telecom C-band at 1540 nm, but they need a sensitizer to enhance absorption. Na^+ substitution for Ag^+ and Bi^{3+} doping at the In^{3+} site is a possible strategy to enhance the broadband emission of $Cs_2AgInCl_6$, which could be used as a sensitizer for energy transfer to rare-earth elements. Herein, self-trapped exciton (STE) energy transfer to Er^{3+} at 1540 nm in double perovskite is reported. An acid precipitation method was used to synthesize $Cs_2AgInCl_6$ and its derivatives with Er^{3+}, Bi^{3+}, and Na^+. Bare $Cs_2AgInCl_6$:Er emission signals were found to be weak at 1540 nm, but Bi^{3+} doping increased them by 12 times, and Bi^{3+} and Na^+ doping increased signal intensity by up to 25 times. Electron paramagnetic resonance spectroscopy characterized a decrease in axial symmetry over the Er^{3+} ions after the substitutions of Na^+ and Bi^{3+} in $Cs_2AgInCl_6$ at low temperatures (<7 K) for the first time. Moreover, an increase in pressure compressed the structure, which tuned the STE transition for free exciton emission, and a further increase in pressure distorted the cubic phase above 70 kbar.

Introduction

Erbium (Er)-doped fiber amplifiers are optical amplifiers used for the C band (1530–1565 nm) and L band (1565–1625 nm) because of the low loss of fiber in long-distance optical communications.[1] However, Er-doped fibers suffer from low absorption and possibly need sensitizers, such as Yb^{3+}, to enhance the emission of Er^{3+} as presented in Fig. 1a.[2] In the present work, a possible self-trapped exciton (STE)-based energy transfer strategy to enhance the emission of Er at 1540 nm is reported as shown in Fig. 1b.

Over the last decade, lead (Pb)-free double perovskites, such as Cs_2AgInX_6, Cs_2AgBiX_6, and $Cs_2NaInCl_6$, have been identified for optoelectronic applications.[3–7] Among them, $Cs_2AgInCl_6$ has attracted more researchers because of its direct bandgap and weak white light emission *via* STE.[8] STE-derived emission is a photoluminescence (PL) mechanism where the exciton emission energy is much smaller than the bandgap of the material.[8] This emission is generally found in halide and organic molecular crystals.[9,10] The STE in $Cs_2AgInCl_6$ nano- and microcrystals is due to the strong Jahn–Teller distortion of the $AgCl_6$ octahedron, which induces parity-forbidden transition.[8] Luo *et al.*[11] broke the inversion symmetry and relaxed the parity-forbidden transition by alloying Na^+ into Bi^{3+} doped $Cs_2AgInCl_6$. The PLQY increased to 86%, and it was applied for white light emission with a single-material LED device. Wang *et al.*[12] used co-doping of Ni^{2+}, Bi^{3+}, and Ce^{3+} into $Cs_2Ag_{0.4}Na_{0.6}InCl_6$ to enhance the PLQY by approximately 98%. They also found *via* density functional theory calculation that doping of Ce^{3+} is responsible for the formation of shallow trapped states. Locaridi *et al.*[13] discovered that the substitution of Ag^+ by Na^+ localized the $AgCl_6$ energy level above the valence band maximum and the $BiCl_6$ state appeared below the conduction band minimum, which was responsible for electron–hole recombination. Zheng *et al.*[14] found that the relaxation in the parity-forbidden transition of $(^1S_0 \rightarrow {}^3P_2)$ of the Bi^{3+} $6s^2$ configuration after Na^+ substitutions at Ag^+ sites enhanced the optical absorption. These results showed that the possible broadband emission is due to STE and that Na^+

[a]Department of Chemistry, National Taiwan University, Taipei 106, Taiwan. E-mail: rsliu@ntu.edu.tw
[b]Nanoscience and Technology Program, Taiwan International Graduate Program, Academia Sinica and National Taiwan University, Taipei 115, Taiwan
[c]Institute of Experimental Physics, Faculty of Mathematics, Physics, and Informatics, University of Gdańsk, 80-308 Gdańsk, Poland
[d]Department of Technical Physics, Faculty of Mechanical Engineering and Mechatronics, West Pomeranian University of Technology in Szczecin, Piastow 48, 70-311 Szczecin, Poland

† Electronic supplementary information (ESI) available. See DOI: https://doi.org/10.1039/d2nr05478g

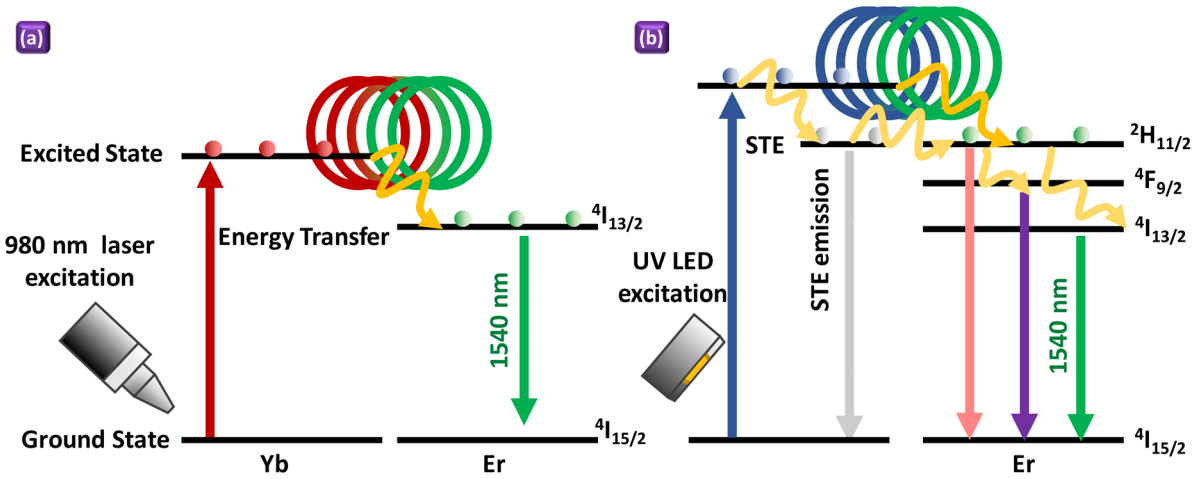

Fig. 1 Energy transfer mechanism of (a) Yb/Er co-doped optical amplifier and (b) STE-Er based energy transfer.

and Bi^{3+} doping enhances the emission intensity and quantum efficiency.

Several research groups recently used rare-earth element doping to explore the emission in near-infrared in the $Cs_2AgInCl_6$ double perovskite system. Afrin *et al.*[15] used Bi^{3+} doping as a sensitizer to transfer energy to Er^{3+} in the $Cs_2AgInCl_6$ double perovskite system for enhanced emission at 1540 nm. Liu *et al.*[16] found that doping of Bi^{3+} enhances $Cs_2AgInCl_6$ STE emission, which transfers the energy to Tb^{3+}. A previous study also confirmed that Na^+ ions remove the parity-forbidden transition, consequently enhancing STE emission.[11] Zhang *et al.*[17] enhanced STE emission through Na^+ ion substitutions in Bi^{3+}–Yb^{3+} co-doped $Cs_2AgInCl_6$, which transfers the energy to the characteristic emission of Yb^{3+}. A recent similar approach, where Ho^{3+}–Bi^{3+} was doped into $Cs_2Ag_{1-x}Na_xInCl_6$, was used, and energy transfer was observed.[18] These results showed that the double perovskite provides an ideal trivalent octahedron site for rare-earth elements, and STE is an impeccable energy transfer channel for these elements. Along with this, advanced characterization techniques like synchrotron X-ray diffraction and electron paramagnetic resonance spectroscopy are also needed to understand the detailed double perovskite system with rare-earth doping as well as high-pressure and high-temperature luminescence studies to discuss the STE-derived emission.

Herein, Er^{3+} is incorporated into three types of double perovskite $Cs_2AgInCl_6$ systems: bare, Bi-doped, and Na, Bi-co-doped, to study the optical properties. These three systems preserved the cubic phase and tuned the optical performances of Er. They have broadband white light emission because of STE, but Bi^{3+} and Na^+ co-doping broke the parity-forbidden selection rule and enhanced the emission intensity. Along with STE emission between 400 and 800 nm, emission at 1540 nm is related to the $^4I_{13/2} \rightarrow {}^4I_{15/2}$ transition in Er^{3+}. The emission intensity is highest in $Cs_2Ag_{0.4}Na_{0.6}In_{0.92}Bi_{0.08}Cl_6$:Er compared with the other two systems. High-pressure Raman spectroscopy shows that the increased pressure is responsible for the phase transformation from the cubic to the tetragonal crystal structure. Besides this change, before the phase transition at lower pressure, a pressure-induced crossover of STE and free exciton (FE) state is observed, resulting in FE emission with a narrower band.

Results and discussion

Acid precipitation method for double perovskite synthesis

An acid precipitation method was used to synthesize Er-doped $Cs_2AgInCl_6$ derivatives after modification of the previously reported method.[19,20] In brief, AgCl/NaCl and $InCl_3/BiCl_3/ErCl_3{\cdot}6H_2O$ were added in stoichiometric ratios in HCl and heated at 70–80 °C for 20 min with continuous stirring. Afterward, CsCl was added, which formed the precipitate immediately, and kept for 20 min with continuous stirring. Next, the precipitate was washed with ethanol and further dried and stored for further characterization.

Synchrotron X-ray diffraction to study the crystal structure

Synchrotron X-ray diffraction (SXRD) was used to understand the crystal structure with more accuracy for $Cs_2AgInCl_6$:Er, $Cs_2AgIn_{0.92}Bi_{0.08}Cl_6$:Er, and $Cs_2Ag_{0.4}Na_{0.6}In_{0.92}Bi_{0.08}Cl_6$:Er as shown in Fig. 2a. All system diffraction peaks were well indexed with the cubic system of the $Fm\bar{3}m$ space group (ICSD 15432). Rietveld refinement was used, as shown in Fig. S1,† to refine the crystal, and <2% AgCl impurities were observed in all systems. The appearance of these impurities may be due to the unreacted AgCl precursor. However, the lattice parameter (a) increased from 10.48 Å for $Cs_2AgInCl_6$:Er to 10.54 Å for $Cs_2Ag_{0.4}Na_{0.6}In_{0.92}Bi_{0.08}Cl_6$:Er as shown in Table S1.† These results indicate that the Na^+ cations randomly substitute for Ag^+ cations as per the previous study.[13] In addition, an increase in the peak intensity of the peak around $2\theta \sim 8°$ of the (111) plane is found in the present study. The increase is due to the Na/Ag composition which occurs through the increase

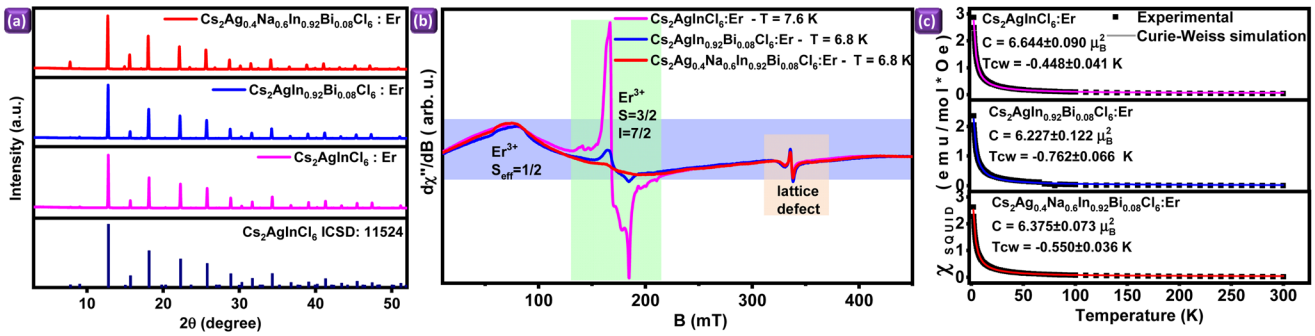

Fig. 2 (a) Synchrotron X-ray diffraction (SXRD) pattern, (b) electron paramagnetic resonance (EPR) spectra, and (c) superconducting quantum interference device (SQUID) of $Cs_2AgInCl_6$:Er, $Cs_2AgIn_{0.92}Bi_{0.08}Cl_6$:Er, and $Cs_2Ag_{0.4}Na_{0.6}In_{0.92}Bi_{0.08}Cl_6$:Er.

in the dispersion factors of Na^+, Ag^+, and In^{3+} with Na alloy in $Cs_2AgIn_{0.92}Bi_{0.08}Cl_6$:Er.[11] The occupancy of Er^{3+} in $Cs_2AgInCl_6$:Er was ~9%, which decreased to ~4% for $Cs_2AgIn_{0.92}Bi_{0.08}Cl_6$:Er and further increased to ~11% for $Cs_2Ag_{0.4}Na_{0.6}In_{0.92}Bi_{0.08}Cl_6$:Er, as shown in Table S2.† These results are similar to the inductively coupled plasma optical emission spectroscopic measurements of the three systems as shown in Table S3.† These outcomes also confirmed that the Na^+ substitution at Ag^+ sites enhances the Er^{3+} occupancy. Along with the crystal structure study, scanning electron microscopy concluded the 6–10 μm size variation in the three systems as shown in Fig. S2.†

Low-temperature electron paramagnetic resonance (EPR) and superconducting quantum interference device (SQUID) magnetometery

The electron paramagnetic resonance (EPR) signal was studied for $Cs_2AgInCl_6$:Er, $Cs_2AgIn_{0.92}Bi_{0.08}Cl_6$:Er, and $Cs_2Ag_{0.4}Na_{0.6}In_{0.92}Bi_{0.08}Cl_6$:Er at a selected temperature of ~7 K, as presented in Fig. 2b, to understand the induced symmetry of paramagnetic ions and crystal lattice defects. As can be seen, the EPR signal originates from several paramagnetic centers. The broad EPR signal observed in a range of up to ~400 mT comes from Er^{3+} ions in low symmetry. This signal is observed for all three compounds. The EPR signal between $120 < B < 220$ mT has a recognizable hyperfine structure that originates from Er^{3+} ions in axial symmetry. This signal appeared in $Cs_2AgInCl_6$:Er with high amplitude but decreased in $Cs_2AgIn_{0.92}Bi_{0.08}Cl_6$:Er and disappeared in $Cs_2Ag_{0.4}Na_{0.6}In_{0.92}Bi_{0.08}Cl_6$:Er (Fig. 2b). We believe that the presence of $BiCl_6$ and $NaCl_6$ octahedra causes a decrease in and then the vanishing of the EPR signal originating from Er^{3+} ions in axial symmetry, respectively. In contrast, the amount of low-symmetry Er^{3+} ions rises, which can be correlated with the SXRD of the incorporation of Bi^{3+} and Na^+ in the $Cs_2AgInCl_6$:Er complex. A weak EPR signal at $B \approx 337$ mT was assigned to electrons trapped on point defects of the $Cs_2AgInCl_6$ crystal lattice. This signal also appeared in the $Cs_2AgIn_{0.92}Bi_{0.08}Cl_6$:Er and $Cs_2Ag_{0.4}Na_{0.6}In_{0.92}Bi_{0.08}Cl_6$:Er systems. More details can be found in the ESI.† The magnetic susceptibility of the three systems was further studied using a superconducting quantum interference device (SQUID) magnetometer in the temperature range of 2–300 K. The SQUID magnetic susceptibility behaves according to the Curie–Weiss equation, whose parameters are Curie–Weiss temperature (TCW) and Curie constant (C). The fits of the Curie–Weiss equation to the experimental data are shown in Fig. 2c. A negative TCW value for all double perovskite systems indicates antiferromagnetic interactions between magnetic ions. The effective magnetic moment (μ_{eff}) for the three systems was determined by applying the Curie constant. The following values were obtained: μ_{eff} ($Cs_2AgInCl_6$:Er) = 7.29μ_B, μ_{eff} ($Cs_2AgIn_{0.92}Bi_{0.08}Cl_6$:Er) = 7.05$\mu_B$, and μ_{eff} ($Cs_2Ag_{0.4}Na_{0.6}In_{0.92}Bi_{0.08}Cl_6$:Er) = 7.14$\mu_B$. The theoretical value of the effective magnetic moment for Er^{3+} ions with a spin of $S = 1/2$ is μ_{eff} = 7.36μ_B. The above-mentioned values of the effective magnetic moment indicate that the dominant signal originates from the Er^{3+} ions with a spin of $S_{eff} = 1/2$. Weak interactions between Er^{3+} ions with a spin of $S_{eff} = 1/2$ may indicate a lack of direct energy transfer between Er^{3+} ions. This can take place through an additional medium, *e.g.* excitons. However, we observed defects of the crystal lattice in the form of trapped electrons in the lattice vacancies, which may constitute this medium.

Photoluminescence study to evaluate STE and infrared emission

Photocurrent excitation (PC), absorbance (ABS), PLE spectra, and PL emission between 400 and 800 nm were used to understand the origin of transition observed in these three systems, as shown in Fig. 3a. A huge Stokes shift characterized the PL due to the STE formation.[11,21] Along with broadband emission, weak line structures related to the typical f–f transitions of Er^{3+} ions were observed at the wavelength ranges of 530–570 and 650–680 nm. A notable detail is that the normalized emissions for all three samples looked similar. However, the intensity varied remarkably from very weak for $Cs_2AgInCl_6$:Er to very strong for $Cs_2Ag_{0.4}Na_{0.6}In_{0.92}Bi_{0.08}Cl_6$:Er as shown in Fig. 3c. A total of two bands in $Cs_2AgInCl_6$:Er and three bands in $Cs_2AgIn_{0.92}Bi_{0.08}Cl_6$:Er and $Cs_2Ag_{0.4}Na_{0.6}In_{0.92}Bi_{0.08}Cl_6$:Er were identified based on a comparison of the ABS, PLE, and PC spectra: (A) an optical band with maxima in the range of 300–350 nm; (B) an optical band at 350–380 absent in $Cs_2AgInCl_6$:Er; and (C) an optical band with maxima in the

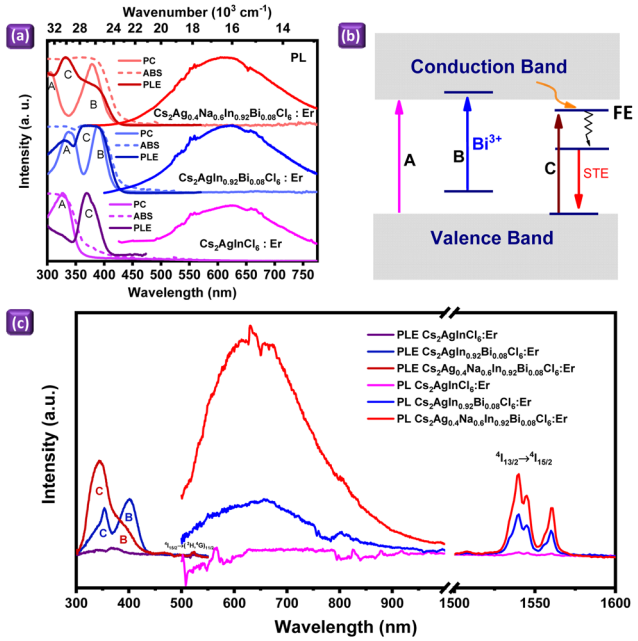

Fig. 3 (a) Photocurrent excitation (PC), absorbance (ABS), photoluminescence excitation (PLE at λ_{em}: 620 nm) and photoluminescence (PL at λ_{ex}: 315 nm) spectra of $Cs_2AgInCl_6$:Er, (pink) $Cs_2AgIn_{0.92}Bi_{0.08}Cl_6$:Er (blue), and $Cs_2Ag_{0.4}Na_{0.6}In_{0.92}Bi_{0.08}Cl_6$:Er (red). (b) The diagram presents a possible transition. (c) PLE (λ_{em}: 1540 nm) and PL (λ_{ex}: 352 nm) spectra of $Cs_2AgInCl_6$:Er, $Cs_2AgIn_{0.92}Bi_{0.08}Cl_6$:Er, and $Cs_2Ag_{0.4}Na_{0.6}In_{0.92}Bi_{0.08}Cl_6$:Er at the emission and excitation wavelengths of 1540 and 352 nm, respectively.

range of 320–380 nm, absent in the PC spectra for all the samples. A simple transition diagram is shown in Fig. 3b, where A is related to the excitation of electrons from the valence band (VB) to the conduction band (CB) and defines the bandgap energy. The B feature is related to the presence of Bi^{3+} in $Cs_2AgIn_{0.92}Bi_{0.08}Cl_6$:Er and $Cs_2Ag_{0.4}Na_{0.6}In_{0.92}Bi_{0.08}Cl_6$:Er. The observed transition may be related to the charge transfer transition (from the ground state of Bi to the conduction band) or that between the local states of bismuth ($^1S_0$–$^3P_1$). However, considering the photocurrent results, the excited state of Bi^{3+} ($^3P_1$) in this case degenerated with the CB. The C features are from the excitation spectra to the direct excitation of the FE state. Due to the rapid relaxation to the lower STE state, FE-related emission was not observed at atmospheric pressure. However, as the pressure increased, the position of the STE state changed, and the transition from the FE state was observed. In this part, the pressure- and temperature-dependent optical studies are discussed further. In addition, the fast relaxation to the STE state resulted in the absence of the C feature in the PC spectra because the exciton binding energy was too large for thermally activated charge generation. The PLE and PL emission spectra were recorded between 400 and 1600 nm and are presented in Fig. 3c. The PL spectra were recorded under 352 nm excitation and the PLE spectra were recorded when 1540 nm emission was observed. $Cs_2AgInCl_6$:Er showed very weak emission at 1540 nm related to the $^4I_{13/2} \rightarrow {}^4I_{15/2}$ Er^{3+} transition and weak STE emission. After the substitution of Bi^{3+} at the In^{3+} site in the $Cs_2AgInCl_6$:Er system, both STE-derived broadband emission around 620 nm and emission at 1540 nm were enhanced. These results are similar to those previously reported, where Bi^{3+}-doped systems had higher emission intensity than the undoped ones.[15] In the extended work, after alloying with Na^+ at the Ag^+ site, the intensity of the broadband STE increased compared with that upon doping with Bi only, which could be attributed to the relaxation in the parity-forbidden transition after the Na^+ alloy.[11] The intensity of the characteristic peak at 1540 nm of $^4I_{13/2} \rightarrow {}^4I_{15/2}$ also increased. As a result, the emission intensity at 1540 nm of $Cs_2Ag_{0.4}Na_{0.6}In_{0.92}Bi_{0.08}Cl_6$:Er was 25 times higher than that of $Cs_2AgInCl_6$:Er and 2 times higher than that of $Cs_2AgIn_{0.92}Bi_{0.08}Cl_6$:Er. The relative enhancement in the PL intensity of Er^{3+} could be attributed to the energy transfer from the STE to Er^{3+} states. Fig. 3c shows the PLE spectra recorded at the emission wavelength of 1540 nm presenting STE-Er^{3+} energy transfer. The excitation spectra of Er^{3+} show the presence of two bands: a (B) optical band with maxima in the range of 350–380 nm and (C) the optical band at 320–380 nm along with an absorption band at 521 nm, which correspond to the $^4I_{15/2} \rightarrow (^2H,{}^4G)_{11/2}$ transition.[22] The B band is related to the presence of Bi^{3+} ions and the C band to the direct absorption of the electron from the valence band to the free exciton state. The B excitation pathway produces the electron for the conduction band and the relaxation of such an excited state could be by electron and hole capture by the FE state, resulting in STE emission and Er^{3+} emission. Along with this, the C excitation pathway produces electrons that excite to the free exciton state and then relax to the STE state. This pathway of STE emission is highly populated and majorly contributes to electron transfer to the excited Er^{3+} states. In addition, the STE emission spectrum is completely overlapped with the absorption of Er^{3+} at 521 nm of the $^4I_{15/2} \rightarrow (^2H,{}^4G)_{11/2}$ transition (see Fig. S4†), thus fulfilling the criteria of the Förster–Dexter theory concerning energy transfer, namely the spectral overlap of the PL of the donor with the absorption of the acceptor.[23,24]

PL decay dynamics were also recorded for all three systems at the excitation wavelength of 352 nm and emission wavelength of 1540 nm as shown in Fig. S5.† $Cs_2AgInCl_6$:Er showed bi-exponential decay with lifetime components of 1.27 and 10.9 ms (average of 9.24 ms). The Laporte parity selection rule of f–f transitions in Er^{3+} ($^4I_{13/2} \rightarrow {}^4I_{15/2}$) causes the optical transitions to be strongly forbidden and, consequently, a lifetime is in milliseconds. $Cs_2AgIn_{0.92}Bi_{0.08}Cl_6$:Er also showed a single exponential decay with a lifetime of 17.9 ms. This result is similar to the previously reported result of the PL decay of Bi^{3+}–Er^{3+} co-doped $Cs_2AgInCl_6$.[15] The $Cs_2Ag_{0.4}Na_{0.6}In_{0.92}Bi_{0.08}Cl_6$:Er system showed a single exponential decay with a lifetime of 18.9 ms. The enhancement in lifetime decay suggested that the Na alloy and Bi-doped $Cs_2AgInCl_6$ system improve the crystalline surrounding the Er^{3+} ions, thus reducing the trap states.[11]

Temperature-dependent photoluminescence study

Next, to evaluate the effect of temperature on the optical properties of $Cs_2Ag_{0.4}Na_{0.6}In_{0.92}Bi_{0.08}Cl_6$:Er, temperature-dependent PLE, PL, and luminescence decay were studied. Fig. 4a presents the temperature-dependent normalized PLE spectra of $Cs_2Ag_{0.4}Na_{0.6}In_{0.92}Bi_{0.08}Cl_6$:Er. At low temperatures, three bands, A, B, and C, appeared. However, with the increase in temperature, the A and B bands diminished and only the C band was present at 500 K. These results confirmed the delocalization of carriers observed in photocurrent measurements, in which after photoexcitation, the electron is transferred to the conduction band and ceases to effectively excite the STE. Fig. 4b presents the temperature dependence of the PL spectra of $Cs_2Ag_{0.4}Na_{0.6}In_{0.92}Bi_{0.08}Cl_6$:Er at temperatures ranging from 80 K up to 440 K, excited by 315 nm UV LEDs. Fig. S6† shows the analogous results of $Cs_2AgInCl_6$:Er and $Cs_2AgIn_{0.92}Bi_{0.08}Cl_6$:Er. The spectra show the temperature evolution of the spectral shape visible as the spectrum shifts towards higher energies and a widening of the bandwidth. The narrow line peaks and dips present in all of the PL spectra are related to Er ions in the lattice resulting from the emission (peaks) or reabsorption (dips) of light. The PL intensity is very sensitive to temperature, as shown by the rapid diminishing of the relative height of the PL spectra when moving from cryogenic temperatures to room temperature. The lifetime decays of $Cs_2Ag_{0.4}Na_{0.6}In_{0.92}Bi_{0.08}Cl_6$:Er (Fig. 4c) and $Cs_2AgInCl_6$:Er and $Cs_2AgIn_{0.92}Bi_{0.08}Cl_6$:Er (Fig. S7a and S7b,† respectively) are also obtained. PL intensity *versus* temperature is calculated by integrating the PL spectra as shown in Fig. 4d for $Cs_2Ag_{0.4}Na_{0.6}In_{0.92}Bi_{0.08}Cl_6$:Er. The dashed lines denote the theoretical approximation of the PL *versus* temperature curve by fitting to a model assuming a single activation barrier ΔE for non-radiative quenching as follows:

$$I(T) = \frac{I_0}{1 + \frac{p_{nr}}{p_r}\exp\left(-\frac{\Delta E}{kT}\right)} \quad (1)$$

where I_0 is the PL intensity at $T \rightarrow 0$ and p_{nr} and p_r are non-radiative and radiative transition probabilities, respectively. The p_r could be taken directly from the low-temperature decay time measurement and it is equal to 12.9 μs. The obtained activation energy ΔE is equal to 2200 cm^{-1} (273 meV), while $p_{nr}/p_r = 1.7 \times 10^4$.

The observed decay profile is non-exponential as shown in Fig. 4c. Therefore, only the average luminescence decay times for the tested materials could be determined. The temperature-dependent luminescence decay curves present the average decay times calculated based on decay curves $I(t)$ from Fig. S7† using eqn (2) as follows:

$$\bar{\tau} = \frac{\int_0^\infty tI(t)\mathrm{d}t}{\int_0^\infty I(t)\mathrm{d}t} \quad (2)$$

The temperature dependence of the average decay time $\bar{\tau}$ presented in Fig. 4d (blue balls) shows that the diminishing of the decay time is a two-step process; the first step engages at the lowest temperatures, while the second activates at *ca.* 200 K. The second shortening process lines up relatively well with the temperature diminishing of the PL intensity shown in Fig. 4d. This finding indicated that the diminishing of the luminescence decay time results from the luminescence quenching process. In the case of $Cs_2Ag_{0.4}Na_{0.6}In_{0.92}Bi_{0.08}Cl_6$:Er at low temperatures, two components are observed in the luminescence decay in Fig. 4c: a short one in the ns range and a long one in the μs range. Using time-resolved spectroscopy at 10 K, careful analysis showed an additional emission at low temperatures. Fig. S8a† presents a streak image of $Cs_2Ag_{0.4}Na_{0.6}In_{0.92}Bi_{0.08}Cl_6$:Er at 10 K showing two distinct luminescence processes, one in the ns time range (orange box) and the other in the μs time range (blue box). Fig. S8b† presents time-resolved emission spectra obtained at time intervals denoted by the boxes in Fig. S8a.† Fig. S8b† shows that the ns emission is prominent. It blue-shifts at low temperatures and then gradually merges with the μs emission spectrum at high temperatures up to 100 K. Above 100 K, such an additional emission becomes unnoticeable. This emission is not related to the FE or STE state and it is probably related to other luminescence centers, such as surface defects.

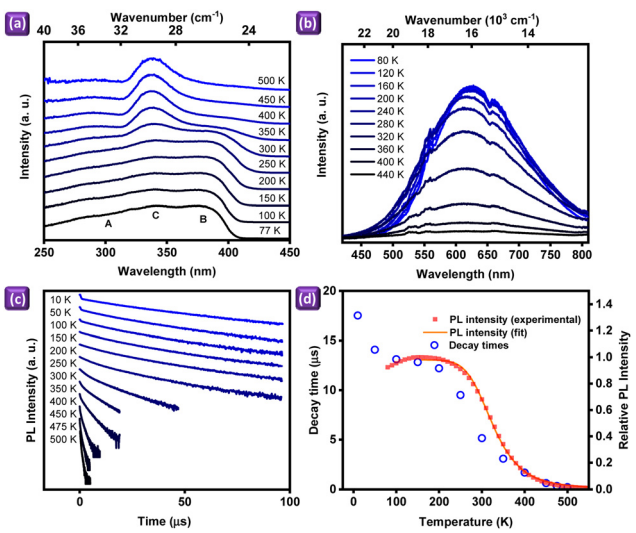

Fig. 4 Temperature-dependent (a) photoluminescence excitation (PLE, λ_{em}: 620 nm), (b) photoluminescence emission (PL, λ_{ex}: 315 nm) spectra, (c) luminescence decay, (d) luminescence intensity *vs.* temperature and theoretical approximation of eqn (1) and (2) for $Cs_2Ag_{0.4}Na_{0.6}In_{0.92}Bi_{0.08}Cl_6$:Er.

Pressure-dependent Raman spectroscopy study

Raman spectroscopy was carried out for all these three systems as shown in Fig. S9,† and *in situ* high-pressure Raman experiments of $Cs_2Ag_{0.4}Na_{0.6}In_{0.92}Bi_{0.08}Cl_6$:Er up to 114 kbar at room temperature were conducted. The lattice vibrations observed in the Raman spectra were affected by the continuous changes in the bond length between the ions in the crystal structure and the abrupt structural changes (phase transitions) under

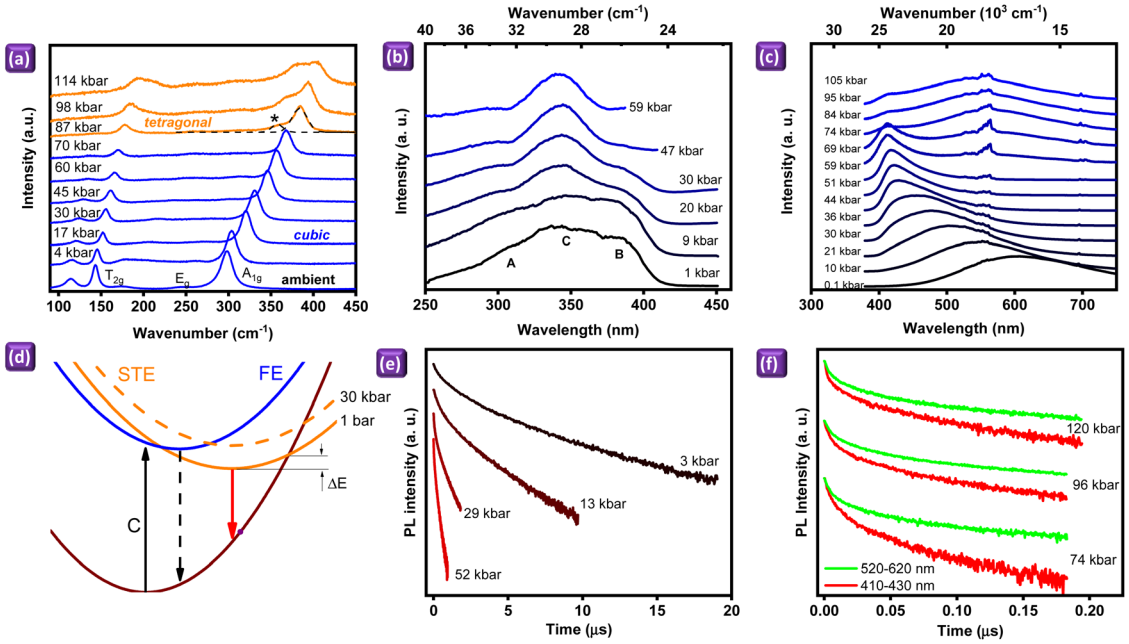

Fig. 5 (a) Raman spectra and (b) photoluminescence excitation and (c) emission of $Cs_2Ag_{0.4}Na_{0.6}In_{0.92}Bi_{0.08}Cl_6$:Er as a function of pressure. (d) The configuration coordination diagram of $Cs_2Ag_{0.4}Na_{0.6}In_{0.92}Bi_{0.08}Cl_6$:Er at ambient and high hydrostatic pressure around 30 kbar. Pressure dependence PL decay curve (e) before and (f) after the phase transition 70 kbar.

pressure. Fig. 5a shows a series of pressure-dependent Raman spectra of $Cs_2Ag_{0.4}Na_{0.6}In_{0.92}Bi_{0.08}Cl_6$:Er. At ambient pressure, $Cs_2Ag_{0.4}Na_{0.6}In_{0.92}Bi_{0.08}Cl_6$:Er possesses a cubic structure with the space group $Fm\bar{3}m$. This double perovskite structure is a network of 3D corner-sharing octahedra, where alternating $(Ag/Na)Cl_6$ and $(In/Bi)Cl_6$ octahedra are arranged in a rock salt configuration with Cs atoms occupying the cubic octahedron cavity.[24] The Raman spectrum consists of three vibration modes below 360 cm^{-1} at ambient conditions. According to the assignment of analogs in previous studies, the bands at 297 and 250 cm^{-1} were assigned to the stretching vibrations of $(Ag/Na)Cl_6$ and $(In/Bi)Cl_6$ octahedra with different vibrational symmetries of E_g and A_{1g}, while the bands observed at 113, 142, and 174 cm^{-1} could be attributed to the breathing vibration with the T_{2g} symmetry of Bi–Cl, Ag–Cl, and In–Cl bonds, respectively.[25–28] The energy of all the Raman peaks increased with pressure. This increase was observed with a slightly different pressure rate for all lines; the most intensive vibration peak A_{1g} increased with a tremendous rate of approximately 1 cm^{-1} $kbar^{-1}$. This finding resulted from the continuous decrease in the bond length in the $(Ag/Na)Cl_6$ and $(In/Bi)Cl_6$ octahedra with pressure. A notable effect occurred above 70 kbar, where a significant change in the Raman line structure was observed. In the pressure range between 70 and 87 kbar, additional peaks appeared in addition to the most intensive vibration peak A_{1g}. Its intensity increased when pressure was further applied. Such Raman changes could indicate a pressure-induced phase transition of $Cs_2Ag_{0.4}Na_{0.6}In_{0.92}Bi_{0.08}Cl_6$:Er above 70 kbar. Zhang *et al.*[25] have shown that the very similar double perovskite $Cs_2AgBiCl_6$ underwent a phase transition from a cubic $Fm\bar{3}m$ to the tetragonal $I4/m$ structure at a pressure of approximately 50 kbar, which was proven by XRD and Raman results under pressure. The phase transition could explain the discontinuous change in the PL spectra at approximately 80 kbar, as presented in Fig. 5c, where the quenching of narrow emission at 400 nm is observed together with the appearance of a new faint luminescence band at 550 nm.

Pressure-dependent photoluminescence study

Fig. 5b and c present the pressure dependence of normalized PLE and PL spectra of $Cs_2Ag_{0.4}Na_{0.6}In_{0.92}Bi_{0.08}Cl_6$:Er. Fig. S10† presents the pressure-dependent PL spectra with retained relative intensity. The pressure-dependent PL spectra are measured at the excitation wavelength of 325 nm, while the observation wavelength for pressure-dependent PLE spectra is set to the maximum of the PL. The PLE spectra revealed a gradual diminishing of the A and B bands relative to the C band. We did not observe any significant shift in the optical band of PLE spectra; however, above 60 kbar pressure the luminescence from the sample became very weak and the PLE spectra could no longer be measured. The pressure-dependent PL spectrum showed the broadband peak center at ~615 nm shifting towards the higher energy, as presented in Fig. 5c. The emission peak shifts towards shorter wavelengths at a rate of 148 cm^{-1} $kbar^{-1}$ within the pressure range of 0.1–44 kbar (black dots in Fig. S11†). Afterward, the emission peak shifts with increasing pressure to 74 kbar at the rate of 33 cm^{-1} $kbar^{-1}$. In addition, the emission becomes gradually narrower throughout the range of 30–50 kbar (red dots in Fig. S11†). Importantly, this change in PL spectrum width is not related

to the phase transition as it occurs below the 74 kbar threshold. The appropriate explanation of this behavior is that the position of the STE state increases with pressure and the FE state becomes the lowest excited state from which emission occurs at around 400 nm. Around the 70–80 kbar threshold, the emission spectrum changes abruptly, with the emission peak returning to 600 nm (however, with much lower intensity) and the smaller constituent remaining at ~400 nm. This finding coincides well with the cubic-to-tetragonal phase transition inferred from the pressure-dependent Raman spectra. It is important to emphasize that the emission at 600 nm in the tetragonal phase above 74 kbar is from an unknown origin and possibly unrelated to the STE. Following the pressure-dependent PL and PLE results, a configurational coordinate diagram of the energy structure of $Cs_2Ag_{0.4}Na_{0.6}In_{0.92}Bi_{0.08}Cl_6$:Er is presented in Fig. 5d. The brown parabola denotes the ground state of the system and the orange parabola shows the STE level characterized by a very strong Stokes shift (the red arrow denotes a radiative transition to the ground state). In the diagram, ΔE denotes the activation energy for non-radiative luminescence quenching due to the crossing of the STE and ground state parabolas. The value of the barrier varies among $Cs_2AgInCl_6$:Er, $Cs_2AgIn_{0.92}Bi_{0.08}Cl_6$:Er, and $Cs_2Ag_{0.4}Na_{0.6}In_{0.92}Bi_{0.08}Cl_6$:Er. The blue parabola presents the FE state, with an arrow labeled as C denoting the direct transition from the ground state to the FE state. The emission from the FE state (dashed arrow) is not observed at ambient pressure due to the direct transfer to the STE state. However, because of the strong pressure, the STE state shifts towards higher energy and, consequently, the FE emission becomes visible at elevated pressure. We have observed a similar transition in our previous study on Bi-doped $Cs_2AgInCl_6$.[21] The pressure-dependent PL decay curves before (a) and after (b) phase transition above 70 kbar are shown in Fig. 5e and f, respectively. A rapid pressure-induced shortening of the decay curves is observed below the 70 kbar threshold and it is related to the approach of the STE state to the FE state. Above the phase transition, the decay time stabilizes. However, the two constituents of the PL spectrum at 410–430 and 500–600 nm show different shapes of decay curves (faster in the former and slower in the latter case). This finding indicates that the two constituents of the PL emission above 70 kbar are not related to a single optical center. Based on Fig. 5e and f, the average decay times were calculated using eqn (2) and are presented in Fig. S12.† The luminescence decay time shortened from the initial 3 μs by more than an order of magnitude before the phase transition and stabilized in the range of 40–60 ns.

Conclusions

In conclusion, STE-derived energy transfer is used in the Er double perovskite complex for the enhancement of emission at 1540 nm by 25 times for optical telecommunication applications. The acid precipitation precursor method is applied to synthesize the three complexes $Cs_2AgInCl_6$:Er, $Cs_2AgIn_{0.92}Bi_{0.08}Cl_6$:Er, and $Cs_2Ag_{0.4}Na_{0.6}In_{0.92}Bi_{0.08}Cl_6$:Er. Synchrotron X-ray diffraction techniques demonstrated the possible incorporation of Na^+, Bi^{3+}, and Er^{3+} co-doping and maintained the cubic phase of $Cs_2AgInCl_6$. Moreover, with the increase in pressure from ambient to 70 kbar, the structure remained cubic. However, the pressure increase split the breathing and stretching modes, thus confirming the distortion in the cubic system. In pressure-dependent PL, the crossover of STE and FE emission was observed at 30 kbar. This study provides insights into the use of double perovskite-based STE-derived energy transfer to Er^{3+}, which could be the lowest use of optical fiber for the entire optical telecommunication wavelength bands.

Conflicts of interest

There are no conflicts to declare.

Acknowledgements

This work was financially supported by the Advanced Research Center of Green Materials Science and Technology from The Featured Area Research Center Program within the framework of the Higher Education Sprout Project by the Ministry of Education (111L9006), the National Science and Technology Council in Taiwan (contracts NSTC 109-2113-M-002-020-MY3, 110-2923-M-002-017-MY3 and 110-2634-F-002-043), the National Science Centre Poland Grant Opus (nos 2016/23/B/ST3/03911 and 2018/31/B/ST4/00924), and the National Centre for Research and Development Poland Grant (no. PL-TW/VIII/1/2021).

References

1 G. P. Agrawal, *Fibre-Optic Communication Systems*, John Wiley & Sons, New Jersey, 4th edn, 2010.
2 A. Polman and F. C. J. M. van Veggel, *J. Opt. Soc. Am. B*, 2004, **21**, 871–892.
3 Y. Bekenstein, J. C. Dahl, J. Huang, W. T. Osowiecki, J. K. Swabeck, E. M. Chan, P. Yang and A. P. Alivisatos, *Nano Lett.*, 2018, **18**, 3502–3508.
4 S. E. Creutz, E. N. Crites, M. C. De Siena and D. R. Gamelin, *Nano Lett.*, 2018, **18**, 1118–1123.
5 Y. Liu, Y. Jing, J. Zhao, Q. Liu and Z. Xia, *Chem. Mater.*, 2019, **31**, 3333–3339.
6 J. C. Dahl, W. T. Osowiecki, Y. Cai, J. K. Swabeck, Y. Bekenstein, M. Asta, E. M. Chan and A. P. Alivisatos, *Chem. Mater.*, 2019, **31**, 3134–3143.
7 B. Yang, F. Hong, J. Chen, Y. Tang, L. Yang, Y. Sang, X. Xia, J. Guo, H. He, S. Yang, W. Deng and K. Han, *Angew. Chem., Int. Ed.*, 2019, **58**, 2278–2283.
8 S. Li, J. Luo, J. Liu and J. Tang, *J. Phys. Chem. Lett.*, 2019, **10**, 1999–2007.

9 R. T. Williams, K. S. Song, W. L. Faust and C. H. Leung, *Phys. Rev. B: Condens. Matter Mater. Phys.*, 1986, **33**, 7232–7240.
10 W. B. Fowler, M. J. Marrone and M. N. Kabler, *Phys. Rev. B: Solid State*, 1973, **8**, 5909–5919.
11 J. Luo, X. Wang, S. Li, J. Liu, Y. Guo, G. Niu, L. Yao, Y. Fu, L. Gao, Q. Dong, C. Zhao, M. Leng, F. Ma, W. Liang, L. Wang, S. Jin, J. Han, L. Zhang, J. Etheridge, J. Wang, Y. Yan, E. H. Sargent and J. Tang, *Nature*, 2018, **563**, 541–545.
12 C. Y. Wang, P. Liang, R. J. Xie, Y. Yao, P. Liu, Y. Yang, J. Hu, L. Shao, X. W. Sun, F. Kang and G. Wei, *Chem. Mater.*, 2020, **32**, 7814–7821.
13 F. Locardi, E. Sartori, J. Buha, J. Zito, M. Prato, V. Pinchetti, M. L. Zaffalon, M. Ferretti, S. Brovelli, I. Infante, L. De Trizio and L. Manna, *ACS Energy Lett.*, 2019, **4**, 1976–1982.
14 W. Zheng, R. Sun, Y. Liu, X. Wang, N. Liu, Y. Ji, L. Wang, H. Liu and Y. Zhang, *ACS Appl. Mater. Interfaces*, 2021, **13**, 6404–6410.
15 H. Arfin, J. Kaur, T. Sheikh, S. Chakraborty and A. Nag, *Angew. Chem., Int. Ed.*, 2020, **59**, 11307–11311.
16 Y. Liu, X. Rong, M. Li, M. S. Molokeev, J. Zhao and Z. Xia, *Angew. Chem., Int. Ed.*, 2020, **59**, 11634–11640.
17 G. Zhang, Y. Wei, P. Dang, H. Xiao, D. Liu, X. Li, Z. Cheng and J. Lin, *Dalton Trans.*, 2020, **49**, 15231–15237.
18 S. Li, Q. Hu, J. Luo, T. Jin, J. Liu, J. Li, Z. Tan, Y. Han, Z. Zheng, T. Zhai, H. Song, L. Gao, G. Niu and J. Tang, *Adv. Opt. Mater.*, 2019, **7**, 1901098.
19 N. K. Nila and A. Nag, *Chem. Commun.*, 2018, **54**, 5205–5208.
20 G. Volonakis, A. A. Haghighirad, R. L. Milot, W. H. Sio, M. R. Filip, B. Wenger, M. B. Johnston, L. M. Herz, H. J. Snaith and F. Giustino, *J. Phys. Chem. Lett.*, 2017, **8**, 772–778.
21 K. Dave, W. T. Huang, T. Leśniewski, A. Lazarowska, D. Jankowski, S. Mahlik and R. S. Liu, *Dalton Trans.*, 2022, **51**, 2026–2032.
22 R. A. Talewar, S. Mahamuda, A. Vyas, A. S. Rao and S. V. Moharil, *J. Alloys Compd.*, 2019, **775**, 810–817.
23 T. Förster, *Ann. Phys.*, 1948, **437**, 55–75.
24 D. L. Dexter, *J. Chem. Phys.*, 1953, **21**, 836–850.
25 L. Zhang, Y. Fang, L. Sui, J. Yan, K. Wang, K. Yuan, W. L. Mao and B. Zou, *ACS Energy Lett.*, 2019, **4**, 2975–2982.
26 H. Siddique, Z. Xu, X. Li, S. Saeed, W. Liang, X. Wang, C. Gao, R. Dai, Z. Wang and Z. Zhang, *J. Phys. Chem. Lett.*, 2020, **11**, 9572–9578.
27 D. Manna, J. Kangsabanik, T. K. Das, D. Das, A. Alam and A. Yella, *J. Phys. Chem. Lett.*, 2020, **11**, 2113–2120.
28 J. A. Steele, P. Puech, M. Keshavarz, R. Yang, S. Banerjee, E. Debroye, C. W. Kim, H. Yuan, N. H. Heo, J. Vanacken, A. Walsh, J. Hofkens and M. B. J. Roeffaers, *ACS Nano*, 2018, **12**, 8081–8090.